ISTITUTO NAZIONALE DI FISICA NUCLEARE

Sezioni di Genova

A NEW SETUP FOR THE UNDERGROUND STUDY OF CAPTURE REACTIONS

P. Cocconi[1], A. Loiano[2], F. Parodi[1], A. Rottura[1], R. Cereseto[1], M. Parodi[1], A. Manco[1], S. Minutoli[1], A. Palmieri[3], F. Siccardi[1]

1) INFN- Sezione di Genova
2) INFN- Sezione di Napoli
3) Seconda Università di Napoli, Dipartimento di Scienze Ambientali

Abstract

For the study of astrophysically relevant capture reactions in the underground laboratory LUNA a new setup of high sensitivity has been implemented. The setup includes a windowless gas target, a 4π BGO summing crystal, and beam calorimeters. The setup has been recently used to measure the $d(p,\gamma)^3He$ cross section for the first time within its solar Gamow peak i.e. down to 2.5 keV c.m. energy. The features of the optimized setup are described.

1. Introduction

It is well known that energy generation in stars occurs via thermonuclear reactions. In the case of the sun it is believed that the energy production occurs via hydrogen burning, i.e. the p-p chain and the CNO cycle [1]. In this framework, an important role is played by nuclear physics: nuclear reaction cross sections $\sigma(E)$ entering solar model calculations are crucial in constraining the branching ratios of the p-p chain and the production of the related solar neutrinos [1]. Unfortunately, due to the Coulomb barrier of the entrance channel, $\sigma(E)$ drops exponentially with decreasing energy E,

$$\sigma(E) = \frac{S(E)}{E} e^{-2\pi\eta} \quad , \qquad (1)$$

where S(E) is the astrophysical S-factor, η the Sommerfeld parameter, $2\pi\eta = 31.29\ Z_1 Z_2$ $(\mu/E)^{1/2}$, Z_1 and Z_2 the integral nuclear charge numbers in the entrance channel, μ the reduced mass in amu units, and E the center-of-mass energy in keV units. Using this expression, the data obtained at higher energy were normally extrapolated to the relevant stellar energies, the Gamow peak.

In order to reduce or eliminate the uncertainties involved in the extrapolation procedures, considerable efforts have been devoted recently to push the experimental limits towards lower energies. The LUNA (Laboratory for Underground Nuclear Astrophysics) facility [2] was installed in the Laboratori Nazionali del Gran Sasso (LNGS) with the initial motivation of measuring a key reaction of the p-p chain, $^3He(^3He,2p)^4He$, within its solar Gamow peak. To achieve this goal, the experimental sensitivity had to be improved by several orders of magnitude in comparison to previous work, both by optimizing accelerator performance and detection efficiency and by minimizing background contributions. The experiment was carried out at the 50 kV accelerator characterized by compactness, small energy spread, and high beam current [2]. The unique feature, however, is the background suppression provided by the 4000 meter water-equivalent shield of the Gran Sasso mountain, which allowed to measure $\sigma(E)$ as low as 0.01 pb [3].

So far, the charged particles producing reactions $^3He(^3He,2p)^4He$ [3] and $d(^3He,p)^4He$ [4] have been studied at LUNA but the future program [5] plans experiments on radiative capture reactions where γ-rays must be detected with high efficiency. The experimental program will be mainly carried out at a new 400 kV accelerator [6] recently installed at LNGS. For the preparation of this program, we designed a windowless gas target matched to a 4π BGO summing crystal and a beam calorimeter. The new setup was tested at the LUNA 50 kV accelerator, where $\sigma(E)$ of $d(p,\gamma)^3He$ could be measured for the first time within its solar Gamow peak [7], i.e. down to E = 2.5 keV. This paper describes the features of this setup.

2. Windowless gas target

A schematic diagram of the windowless gas target is shown in figure 1. The ion beam enters the target chamber through 3 apertures of high gas flow impedance (A$_3$ to A$_1$, figure 1) and is stopped in a beam calorimeter placed at the downstream part of the chamber. The chamber is designed to fit inside the central hole (diameter $\phi = 6$ cm) of a BGO crystal

(section 4). The target chamber has one port for gas inlet and one extended port for pressure measurement: a Cu pipe of 30 cm length and 6 mm inner diameter leading from the target chamber to a space outside the BGO crystal. The pressure measurement is carried out with a Baratron capacitance manometer (MKS, model 127) to an accuracy of better 1%; the measurement is absolute and independent of the gas used. The gas flow through the water-cooled aperture A1 (ϕ = 7 mm, length L= 40 mm) was pumped by a windowless gas target system with 3 pumping stages consisting of turbo pumps (TV1000 and TV1500, pumping speed = 1000 and 1500 l/s, respectively). The gas flow from the turbo pumps is compressed by a double-stage Roots blower (WS152, pumping speed = 152 m^3/h), cleaned using a zeolite adsorption trap (cooled to liquid nitrogen temperature) and fed back into the target chamber. Fresh gas can be filled into the system from a reservoir. The pumping stages are separated by the apertures A_2 (ϕ = 20 mm, L = 80 mm) and A_3 (ϕ = 25 mm, L = 80 mm), where the pressure in the stages was measured using Penning and Pirani manometers. For D_2 gas of P_0 = 0.5 mbar pressure in the target chamber, the pumping system reduced the pressure to about 10^{-4}, 10^{-6} and 10^{-7} mbar in the respective regions between A_1 and A_2, A_2 and A_3, and upstream of A_3. A similar reduction was observed for other P_0 values and target gases. The pressure P_0 is kept constant using a needle valve (MKS, model 248A) in combination with an electronic regulation unit.

In order to test the homogeneity of the pressure inside the 10 cm long target zone of the target chamber (i.e. the distance between aperture A_1 and the beam calorimeter) and to control possible pressure gradients along the 30 cm long pipe-connection to the Baratron, a dedicated set-up was used (figure 2), where the pressure was measured at 4 positions along the target zone (positions a,b,c, and d): no deviations greater than 0.5% have been observed in the pressure range P_0 = 0.1 to 0.5 mbar.

The pressure drop between the target chamber and the first pumping stage is critical since capture reactions occurring in this segment of the beam line produce γ-rays which can be detected by the BGO crystal within its solid angle. Moreover, these γ-rays cannot be resolved from those produced inside the target chamber. This additional γ-ray flux is proportional, at a given beam energy, to the product of the beam current in the first pumping stage with the gas pressure profile in this zone. In the dedicated setup (figure 2), the pressure profile was observed at the positions A and B for D_2 and N_2 gas. The data (figure 3) have been used in Monte Carlo simulations. For the d(p,γ)^{3}He experiment [7], the percentage of 5.5 MeV γ-rays emitted in the first pumping stage and detected by the BGO crystal relative to the total number of detected γ-rays is 0.5%, 0.8%, and 1.6% for P_0 = 0.1, 0.2, and 0.3 mbar, respectively.

3. *Beam calorimeters*

When an ion beam passes through a gas target, the ion charge state fluctuates [8] preventing a precise ion current measurement. Instead, the current can be determined using a beam calorimeter with a constant temperature gradient between a hot and a cold side, whith respective temperatures T_h and T_c [1,9]. The heating power needed to maintain the hot side at T_h temperature, W_{zero}, is provided by a heater (power transistor and/or thermoresistors) controlled by a feedback circuit. When the ion beam of power W_{beam} = $N_p E_{cal}$ hits the hot side, it contributes to its heating and reduces correspondingly the electric heating power, W_{run}, needed during the beam-on run. Thus, the number of

projectiles N_p impinging on the calorimeter is given by the difference in heating powers without and with beam,

$$N_p = \frac{W_{beam}}{E_{cal}} = \frac{(W_{zero} - W_{run})}{E_{cal}} \,, \qquad (2)$$

where E_{cal} is the kinetic energy of the projectiles arriving at the hot side of the calorimeter. This energy is obtained [10] from the original beam energy minus the kinetic energy lost by the beam in the target gas and calculated from stopping power compilations [11]. Note that this method is independent of the type of gas and the value of the gas pressure as long as both quantities are constant during the runs. With decreasing beam energy and the concurrent decreasing beam current (due to a reduced beam transmittance into the target chamber) the beam power W_{beam} is also reduced leading eventually to the situation $W_{zero} \approx W_{run}$ with an associated large uncertainty in N_p. To improve this situation, beam calorimeters with different heating powers W_{zero} should be available.

For this reason, we built 3 calorimeters with $W_{zero} \cong 4$, 20 and 200 W (in vacuum), where a given calorimeter is installed at the downstream part of the gas target chamber (figure 1). At a given gas pressure in the target chamber, W_{zero} depends on T_h, T_c, and the thermic resistance between the hot and cold sides. We chose $T_h = 60$ °C to prevent a possible overheating of the BGO crystal which is in contact with the vacuum chamber housing the calorimeter (figure 1). The cold side is maintained at $T_c = 0$ °C using a cooling circuit connected to a refrigerator (cooling capacity = 500 W, temperature stability = 0.01 °C). The temperatures are monitored via PT100 thermoresistors with a precision of 0.1 °C: two or three PT100 on the hot side and one PT100 on the cold side of the calorimeter. Differences among the 3 calorimeters are in the thermic resistance and in the geometry of the hot side (i.e. the thickness of a 48 mm diameter Cu disk) as well as in the electric heating of the hot side. Note that the diameter of the Cu disk is much larger than the beam diameter (less than 10 mm) arriving at the hot side of the calorimeter (including angle straggling of the beam in the target gas).

The electronics used for the 4 and 20 W calorimeters is shown schematically in figure 4. A TIP141 Darlington power transistor ($I_{cmax} = 10$ A, $W_{max} = 125$ W) and two parallel resistors (20 Ω, 30 W each) are mounted near the hot side of the calorimeter (the beam stop). The power delivered by the heater is the product of the voltage applied to the transistor emitter (24 V DC) and the current flow in the circuit. This flow can be controlled by varying the emitter-to-base voltage through a control current fed into an operational amplifier with unit gain (figure 4). The current flowing through the transistor and the two resistors is measured by a Hall effect transducer (maximum input current = 5 A, attenuation factor = 200, accuracy = 0.6%). One PT100 sensor is mounted in the center and one at the edge of the 3 mm thick beam stop. With this configuration a 0.005 W heating power stability has been obtained.

The beam stop (hot side) of the 200 W calorimeter has a thickness of 41 mm (figure 5), where 8 resistors (25 Ω, 50 W each) are mounted on the downstream part. The resistors are electrically connected in parallel and can deliver a maximum power of 400 W to a material at 25 °C. The current through the resistors is provided by a standard DC power supply (32 V, 10 A) controlled externally by a 0-10 V signal. With this arrangement the heating power stability is 0.1 W. The temperature T_h is controlled here by 3 PT100 thermoresistors (figure 5).

The feedback control is performed by a PC through a LABVIEW program. We utilized some input/output modules (FIELD POINTS, National Instruments) positioned near the calorimeter and connected to a Windows PC through a RS232 serial port. The LABVIEW program reads the hot and cold side temperatures (PT100 outputs) and produces the heater DC control signal. The feedback is realized with a digital first-order control (PID virtual instruments, National Instruments library) whose parameters have been optimized for each calorimeter. With a rapid change in the power delivered to the calorimeter hot-side (typically when the beam is switched on) the temperature is brought back to the set-point temperature (60 °C) within 3 minutes. The program reads the Hall transducer output signal and the power supply voltage (through a calibrated voltage divider) to deduce the actual power delivered by the heater. The input/output signals are read/varied by the program each second while all parameters (cold and hot side temperatures, heating power, control signals, gas pressure in the target chamber) are saved on a ASCII file at fixed periods (typically each 5 s). The time trends of all parameters are also displayed on the PC screen and allow a continuous monitoring during the runs. In particular, gas pressure in the target chamber must be monitored since its variation could affect the W_{zero} value at the set-point temperature.

For calibration purposes, the calorimeters have been designed to work both as calorimeters and as Faraday cups. The calorimeter and the target chamber are electrically insulated from the upstream parts by a 10 mm thick Teflon disk with a $\phi = 12$ mm central hole; furthermore, an insulating cooling liquid (Julabo, Thermal HY) is used at the cold side and a mylar foil is inserted between the vacuum chamber and the BGO crystal. During the calibration, the calorimeter and the target chamber are connected together to form the Faraday cup. A metallic ring, at -100 V, is inserted in the Teflon insulator to minimize the effects of secondary electrons. At a basis pressure of 5×10^{-5} mbar in the target chamber (where no fluctuations in beam charge are expected), both the collected electric charge of the beam and the power delivered by the heater are measured, where the charge has been measured by a standard current integrator (EG&G, model 439). A typical calibration curve is shown in figure 6. We have repeated the calibration several times over a nine months period with reproducible results, i.e. within a 1% systematic uncertainty.

4. The 4π BGO summing crystal

The BGO crystal (manufactured by Scionix, Netherlands) is a cylinder 28 cm long with a coaxial hole of $\phi = 6$ cm diameter and a radial thickness of 7 cm. The crystal is optically divided in 6 sectors, each covering a 60° azimuthal angle. Two Hamamatsu R1847-07 photomultipliers (PMTs) are coupled to the opposite sides of each sector and can be read in coincidence, reducing the electronic noise. Summing the light produced in all 6 sectors allows to recover the full energy of detected γ-rays. This summing also increases the detection efficiency in the case of γ-ray cascades, leading with high probability to a summing peak of the γ-ray energies. On the other hand, the optical separation of each sector and the time analysis of counts facilitate pile-up rejection (section 5).

The BGO energy resolution, $\Delta E_\gamma/E_\gamma$ has been measured with ^{137}Cs and ^{22}Na γ-ray sources placed in the central hole of the detector: $\Delta E_\gamma/E_\gamma = 17\%$ and 12% for $E_\gamma = 661$ keV and 1274 keV, respectively. The longitudinal homogeneity in light collection was tested by moving the ^{22}Na source along the detector axis: from the pulse height of the γ-rays at 511 keV and 1274 keV in the spectra of each sector including five different positions along

the axis, the light collection was found to be homogeneous within statistical error (typically 3-5%). The detection efficiency, for γ-rays produced inside the detector central hole, is relatively high due to the large solid angle (nearly 4π) and the large crystal thickness. Its actual value depends, of course, on the pressure profile in the gas target system. For the 5.5 MeV γ-rays produced in $d(p,\gamma)^3$He and the D_2 pressure profile shown in figure 3, the detection efficiency was about 70% [7]. This efficiency includes the "add-back" effect of γ-rays releasing their energy in two or more sections of the BGO. By comparing the sum of the individual sector γ-ray spectra with the total energy spectrum obtained adding up the signals from all sectors, a 12% increase in peak detection efficiency has been estimated for the 5.5 MeV γ-ray produced by $d(p,\gamma)^3$He.

Figure 7 shows the peak detection efficiency calculated by the LUNA Monte Carlo code [10] for point-like monochromatic γ-ray sources at the center of the BGO crystal. The precision in detection efficiency is affected by a 1% systematic uncertainty, mainly due to approximations in the description of the set-up geometry.

The natural shield of rocks above LNGS produces a large reduction of background due to cosmic rays. The background due to natural radioactive isotopes, visible in the BGO spectra up to γ-ray energies of about 3 MeV (figure 8), is induced mainly by ^{40}K and Ra daughters and could be reduced by a factor 4 using a passive shielding of lead (thickness = 10 cm). When these sources (cosmic rays and natural isotopes) of background have been attenuated, the BGO spectra showed traces of an intrinsic radioactivity, attributed to the presence of ^{207}Bi [12], coming e.g. from the capture of cosmic protons by ^{206}Pb, which in turn decays, with a mean-life of 38 y into ^{207}Pb. The main γ-rays of ^{207}Pb are E_γ = 570 (10%), 1063 (7%) and 1633 (7%) keV. Such kind of contamination, present in the raw material of the BGO crystal, has been found to be somewhat different in the 6 sectors. It should be noted that the intrinsic contamination, which can not be removed by usual passive or active methods, influences not only the detection limit of γ-rays up to E_γ = 1.6 MeV, but it can give contributions as pile-up signals at higher γ-ray energies. However, this background can be reduced electronically (section 5). Table 1 summarizes the results of a series of measurements performed to study various components of the background. In particular, counts per hour and per keV for the sum signal of the 6 BGO sectors are reported relatively to 3 regions of interest of the spectra (see also figure 8):

• $1.2 \le E_\gamma(\text{MeV}) \le 2.8$: the zone of natural isotopes, nearly unaffected by the shielding of the LNGS mountain;

• $2.8 \le E_\gamma(\text{MeV}) \le 7.0$: the γ-ray energy region of interest for reactions such as $d(p,\gamma)^3$He and ^{14}N$(p,\gamma)^{15}$O; this zone of the spectrum is not influenced by the radioactivity of the rocks but could be influenced by pile-up effects;

• $E_\gamma(\text{MeV}) \ge 7.0$: the zone of cosmic rays where the background reduction in LNGS (a factor 10^6 for cosmic ray flow) can be particularly appreciated.

5. Electronics and data acquisition

The BGO summing crystal is connected to the electronic chain shown in figure 9. The signals from the 12 PMTs are sent to a 16-fold amplifier (CAEN, module N568) which produces, for each incoming pulse, a linear output signal sent to a 16-bit ADC (Silena FAIR, module 9418V). The amplifier produces also for each incoming signal a fast output signal, which is used to generate an acquisition trigger via a constant fraction discriminator

(EG&G, module CF8000).The acquisition trigger must fulfill two conditions: (i) the fast signal from each PMT must be higher than a chosen threshold value, and (ii) the fast signal from a given PMT must be in coincidence with the fast signal from the partner PMT of the same BGO sector, which reduced the possibility to trigger on electronic noise. When at least one sector generates a trigger signal fulfilling these two conditions, the signals arriving from all the 12 PMTs are converted by the ADC. The handling of this electronic steps is performed by a logical OR unit. The coincidence signals between the PMT pairs of each sector are also sent to a scaler module (FAIR SCM) producing a pattern function to record the structure of the acquired event, i. e. it provides an information of the individual sectors involved in the accepted event (resolution time < 100 ns). The total processing time of an event is 19 μs.

The comparison between the pattern and the number of signals converted by the ADC reveals the occurrence of pile-up signals, when the spurious signal is created by a sector different from that producing the trigger. In this case, if the pattern is n-fold and the total number of converted signals is greater than n, this event is rejected in the off-line data analysis. In the case that the pile-up event occurs in the same PMT pair producing also the trigger signal, a simple circuit (figure 10) has been used. The trigger signal (60 ns long) from the OR unit is sent to the start-input of a time-to-amplitude converter (TAC). It is also delayed by 110 ns, stretched up to 4 μs, and then sent to the stop-input of the TAC (4 μs time range). With no pile-up signals present, there is no output from the TAC. However, for a pile-up signal created after the trigger signal, the TAC provides an output signal. The TAC spectrum is thus used to reject such pile-up events in the play-back data analysis.

The data acquisition is based on a mixed FAIR-VME bus [13]. The spectra of the BGO sectors are displayed on-line on a PC screen, while the raw data (i.e. the 12 PMT signals for each trigger, the pile-up pattern, and the TAC spectrum) are saved on a DLT tape for each trigger for play-back data analysis. This analysis includes also summing of the signals from the 6 sectors to arrive at the total γ-ray energy deposited in the BGO crystal.

6. Conclusions

A new setup for the study of radiative capture reactions relevant to nuclear astrophysics has been implemented for the LUNA research program at LNGS. The setup is based on a 4π BGO summing crystal and a windowless gas-target system with the target chamber placed inside the detector central hole. A calorimeter for beam current measurement is also contained inside the same detector. The setup has been recently used for the first measurement of the $d(p,\gamma)^3He$ within its solar Gamow peak [7] and it will be used in the near future for the study of radiative capture reactions such as $^{14}N(p,\gamma)^{15}O$.

Acknowledgments

References

[1] C. Rolfs and W.S. Rodney, *Cauldrons in the Cosmos*, University of Chicago Press, 1988

[2] U. Greife et al., Nucl. Instr. Meth. A350 (1994)327

[3] R. Bonetti et al., Phys. Rev. Lett. 82 (1999) 5205

[4] H. Costantini et al., Phys. Lett. B 482 (2000) 43

[5] P. Prati et al., Nucl. Phys. A654 (1999)920c

[6] A. Formicola et al., to be submitted to Nucl. Instr. Meth. A.

[7] C. Casella et al., First measurement of the $d(p,\gamma)^3$He cross section down to the solar Gamow peak, Nucl. Phys. A. (in press)

[8] S. K. Allison, Rev. of Mod. Phys.. 30 (1958)1138

[9] A. Vlieks, M. Hilgemeier and C. Rolfs, Nucl. Instr. Meth. 213 (1983) 291

[10] C. Arpesella et al., Nucl. Instr. Meth. A360 (1995)607

[11] J. F. Ziegler, *Program TRIM-91, The Transport of Ions in Matter*, IBM Research, New York, 1991

[12] T.A.Lewis, Nucl. Instr. Meth. A264 (1988) 534

[13] A. Ordine et al., IEEE Trans. on Nucl. Science , vol. 45, n. 3, june 1998

Figure Captions

Figure 1 : Schematic diagram of the windowless gas target system. The third pumping stage, upstream of aperture A3, is not shown since it is included in the vacuum system of the LUNA 50 kV accelerator [2]

Figure 2: The dedicated setup for pressure profile measurement: the positions of the port to measure the pressure homogeneity in the target chamber (a,b,c,d) and the pressure gradients in the first pumping stage (A,B) are indicated. The given lengths are in units of mm.

Figure 3: Ratio of target chamber pressure (P_0) over 1st pumping stage (P_1) pressure, measured with D_2 (top) and N_2 (bottom), in two points (A: open squares, B: open circles) of the vacuum line with the dedicated setup shown in figure 2.

Figure 4: Electronics of the heater for the 4 and 20 W calorimeters. The components in the dashed rectangle are mounted near the hot side of the calorimeter. The resistor values are in units of ohm, the capacitances in units of farad, and the voltages in units of volt.

Figure 5: Downstream (left panel) view and section (right panel) of the beam stop (hot side) of the 200 W calorimeter: the positions of resistors (black rectangles) and PT100s (black circles) are shown. All lengths are in units of mm.

Figure 6: A calibration curve of the 4 W calorimeter used for the $d(p,\gamma)^3He$ experiment [7], where the x-axis gives the beam power deduced from the Faraday cup measurement and the y-axis the corresponding beam power deduced from the calorimeter.

Figure 7: Peak detection efficiency calculated by the LUNA Monte Carlo code [10] for monochromatic point-like γ-ray sources at the center of the BGO crystal.

Figure 8: BGO background spectra measured inside and outside the LNGS underground laboratory for a running time of 24 h.

Figure 9: Scheme of the electronic chain connected to the BGO crystal.

Figure 10: Circuit of the TAC based pile-up rejection.

Table 1: Background counting rates measured with the BGO summing crystal in various conditions.

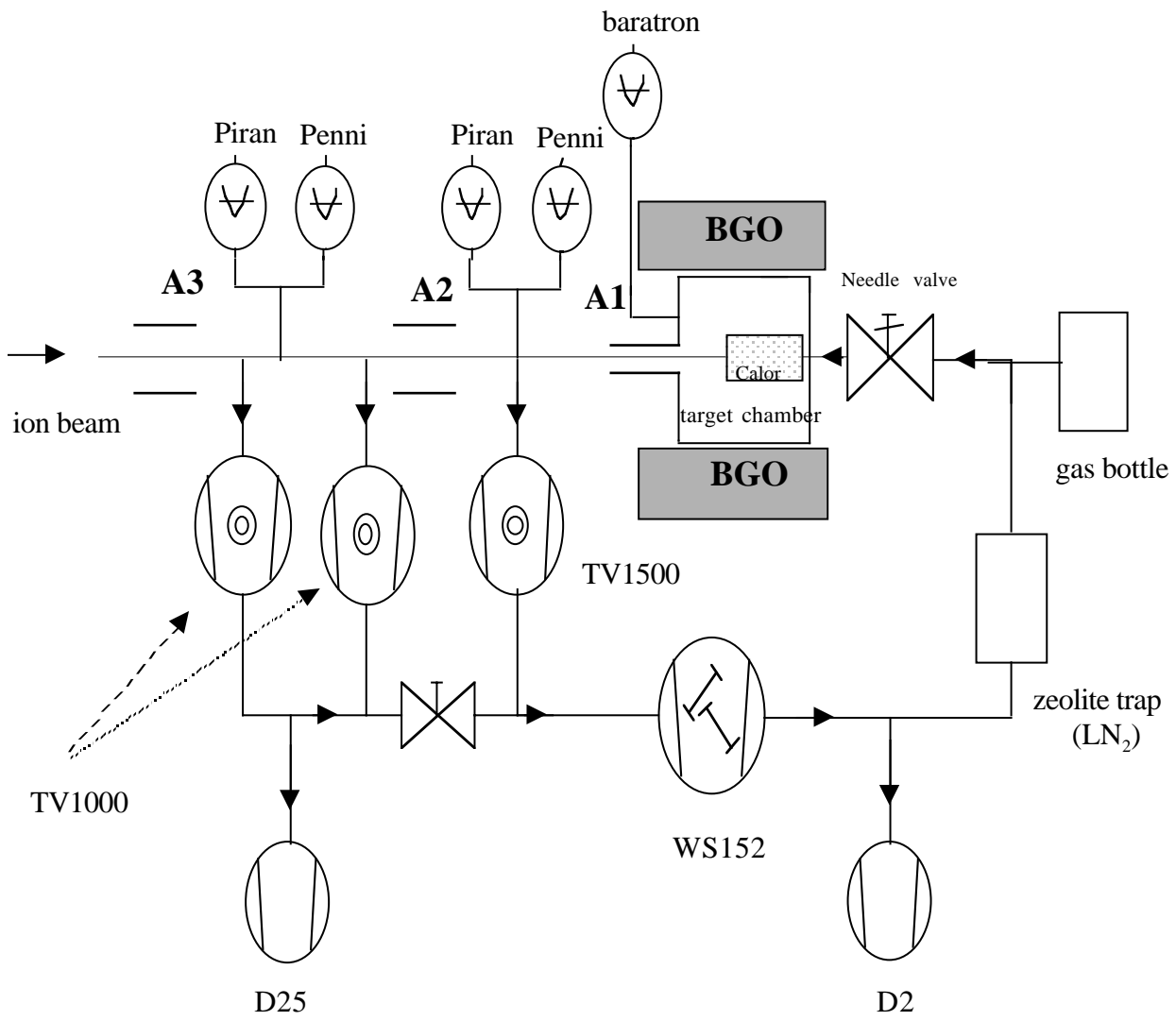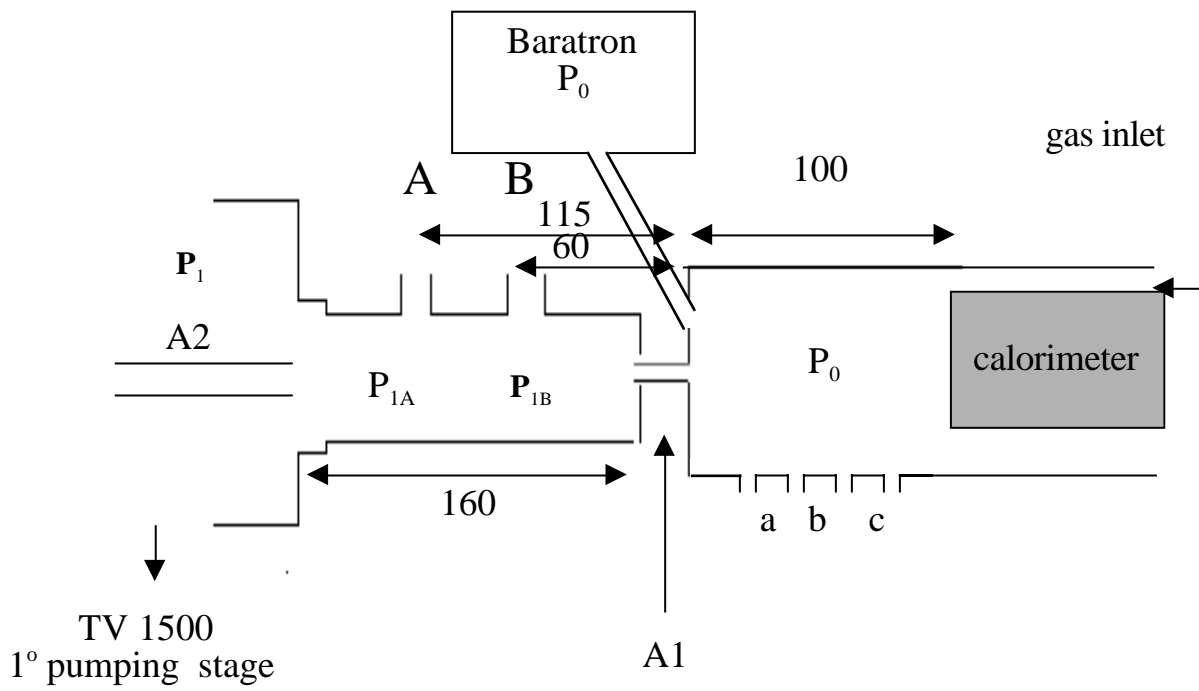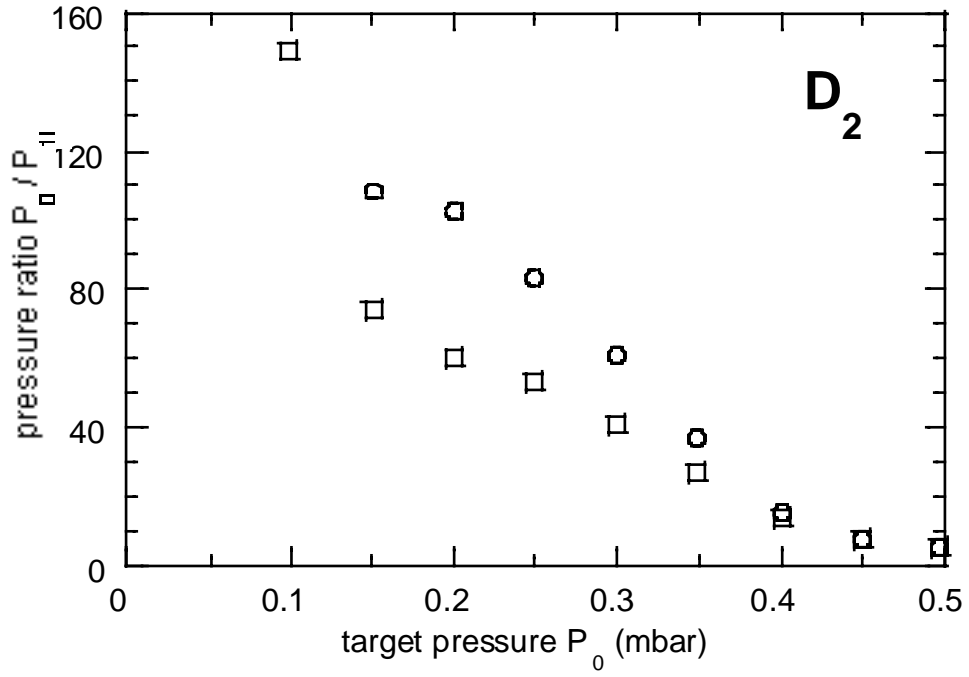| Measurement condition	E = 1.2–2.8 MeV (counts/h/keV)	E = 2.8–7.0 MeV (counts/h/keV)	E > 7.0 MeV (counts/h/keV)
Earth surface, without lead shielding	292	5.85	2.28
Earth surface , with lead shielding	85	3.57	1.89
Underground, without lead shielding	245	0.45	<0.0002
Underground, with lead shielding	60	0.18	<0.0001

baratron

Piran Penni   Piran Penni

A3   **A2**   **A1**

BGO

Needle   valve

ion beam

Calor

target chamber

gas bottle

BGO

TV1500

TV1000

zeolite trap
(LN$_2$)

WS152

D25

D2

Figure 1

Figure 2

Figure 3

From
LabView
control

+24

1 k

1 k

100

MC33072

+

−

-12

100

1 μ 1 μ

TIP141

20 20

HALL
TRANSDUCER

+15
-15

100

To
LabView
control
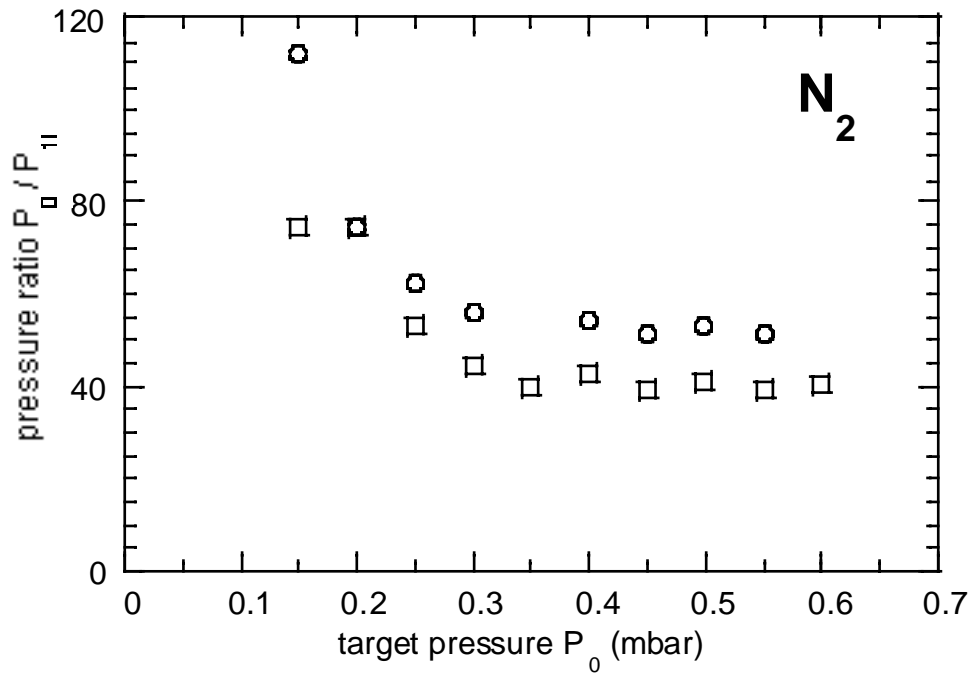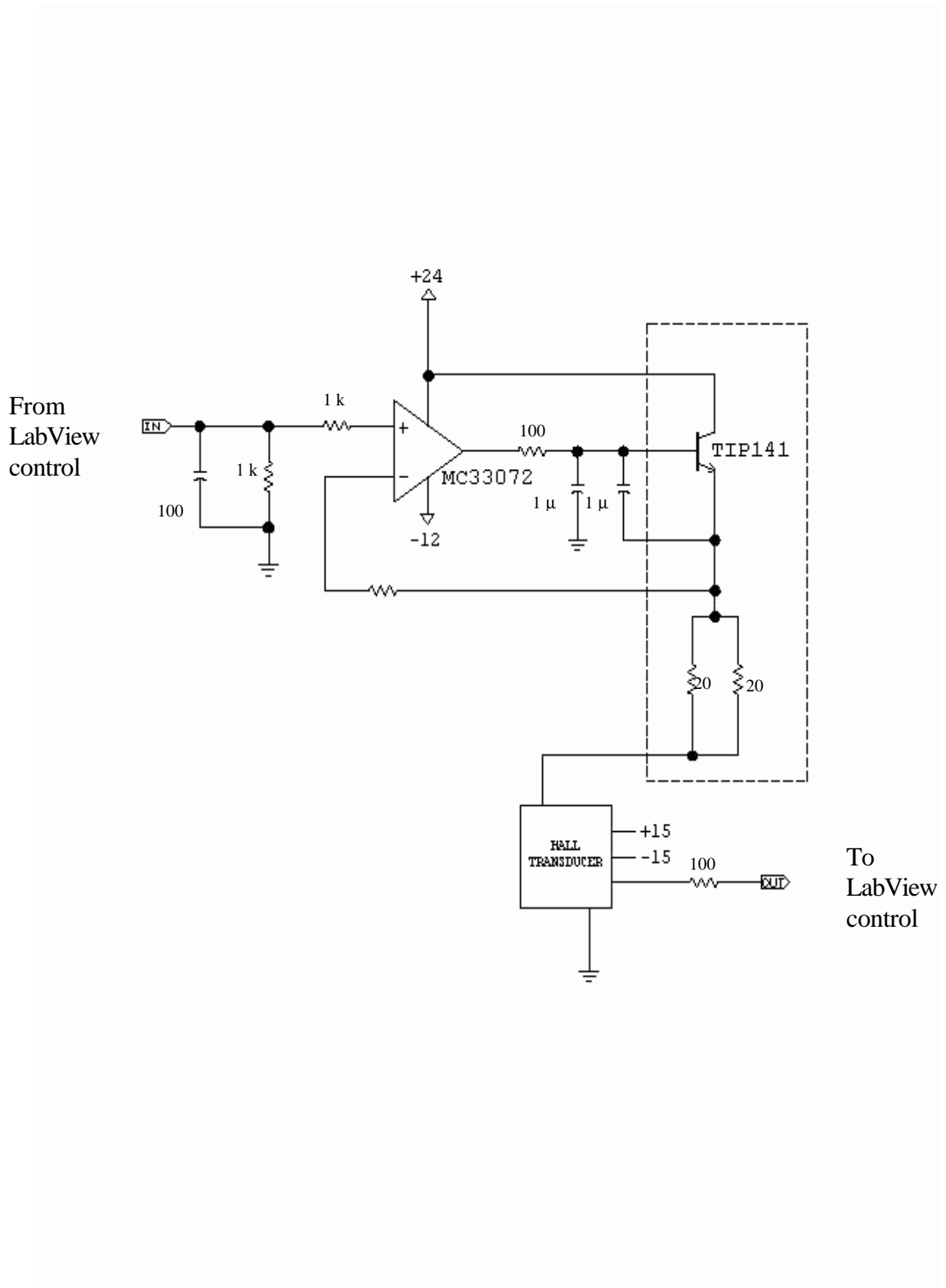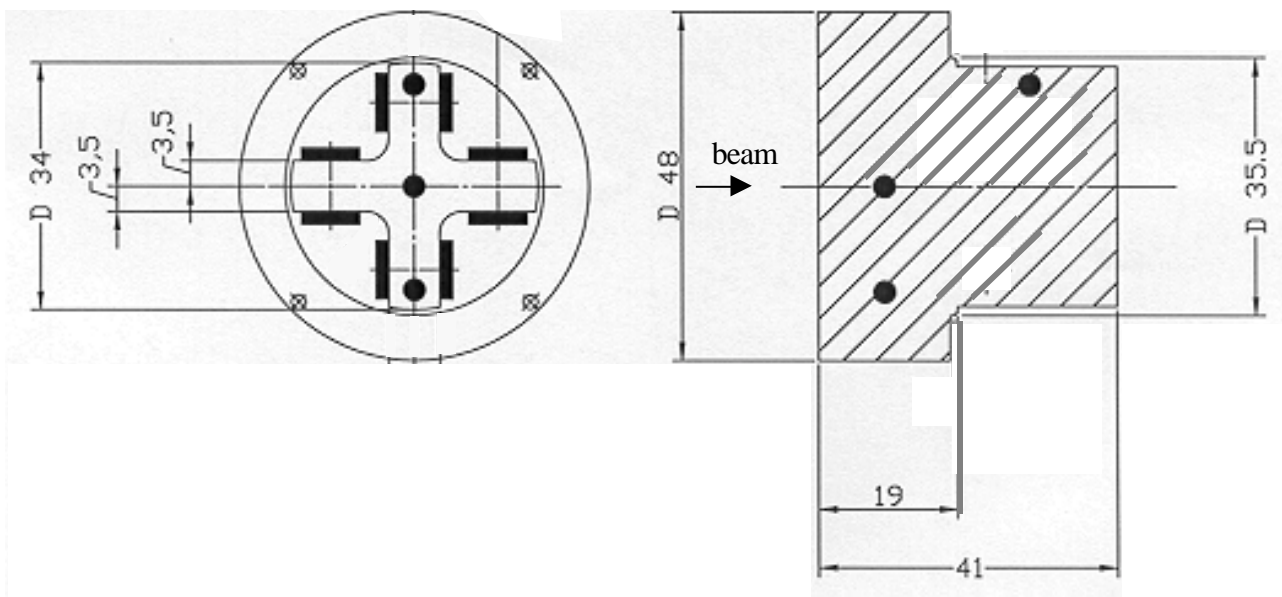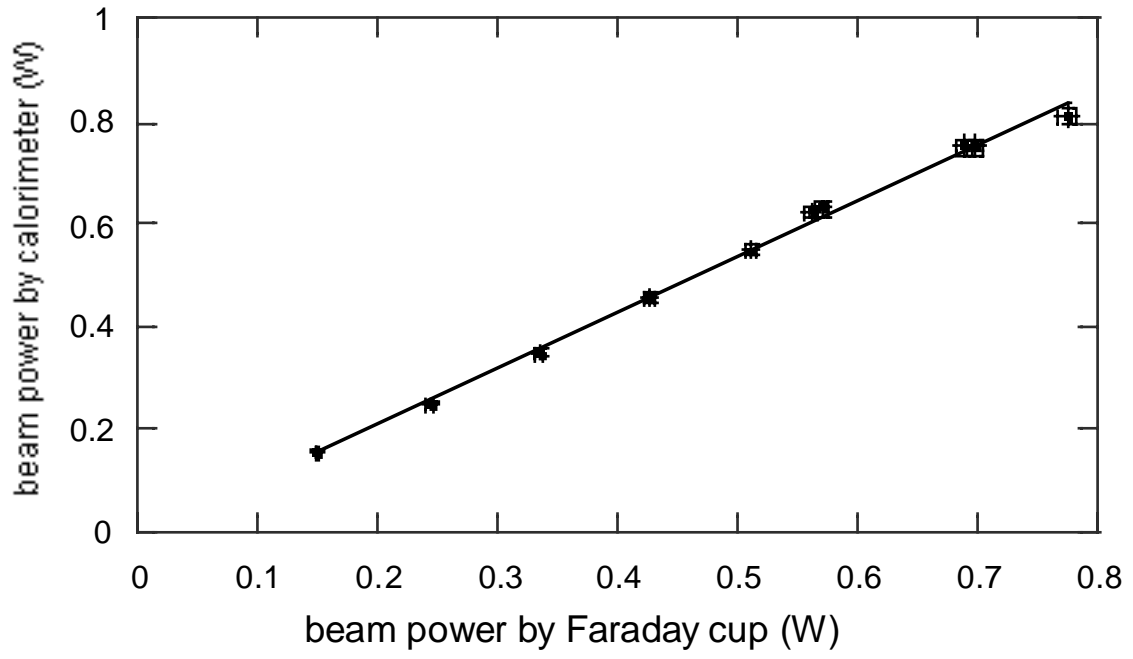
Figure 4

Figure 5

Figure 6
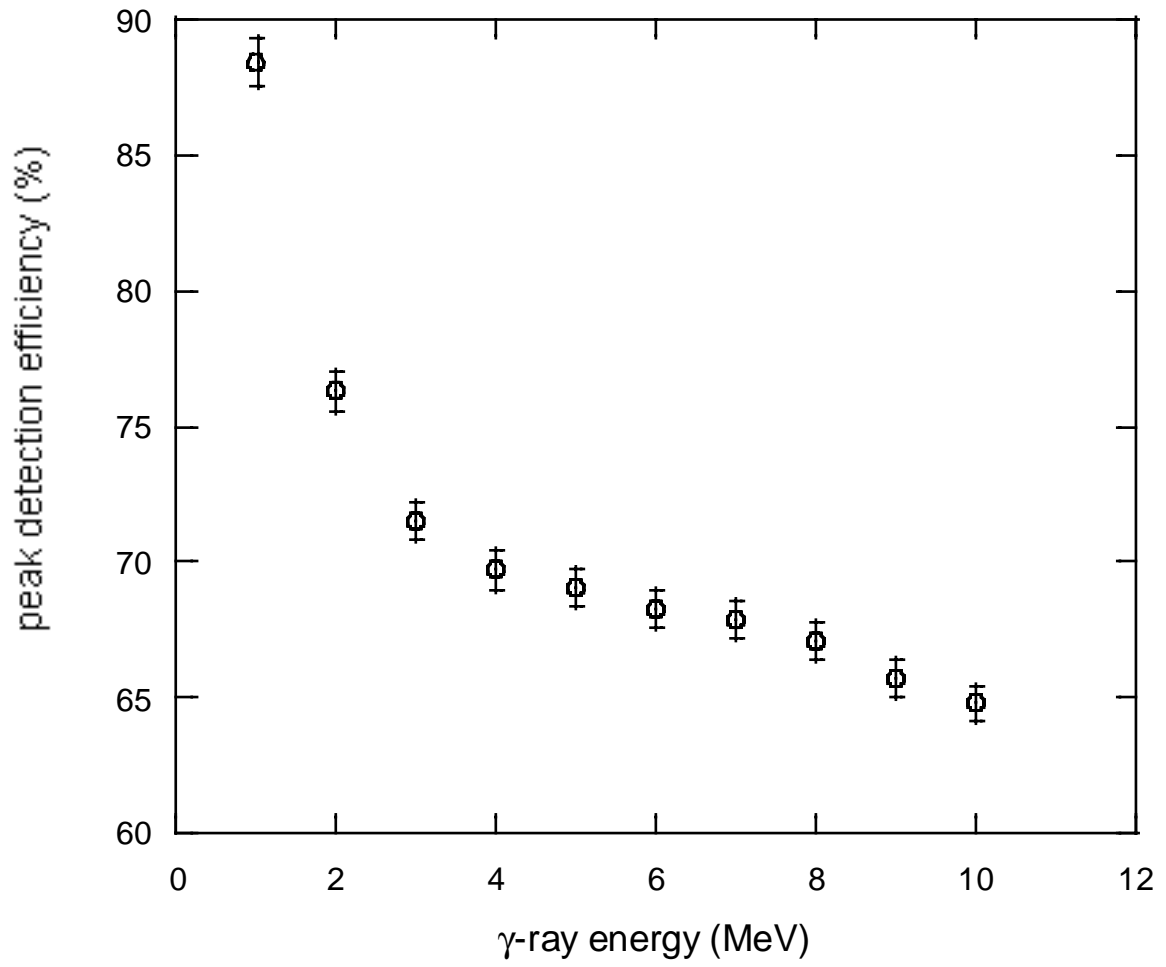
Figure 7
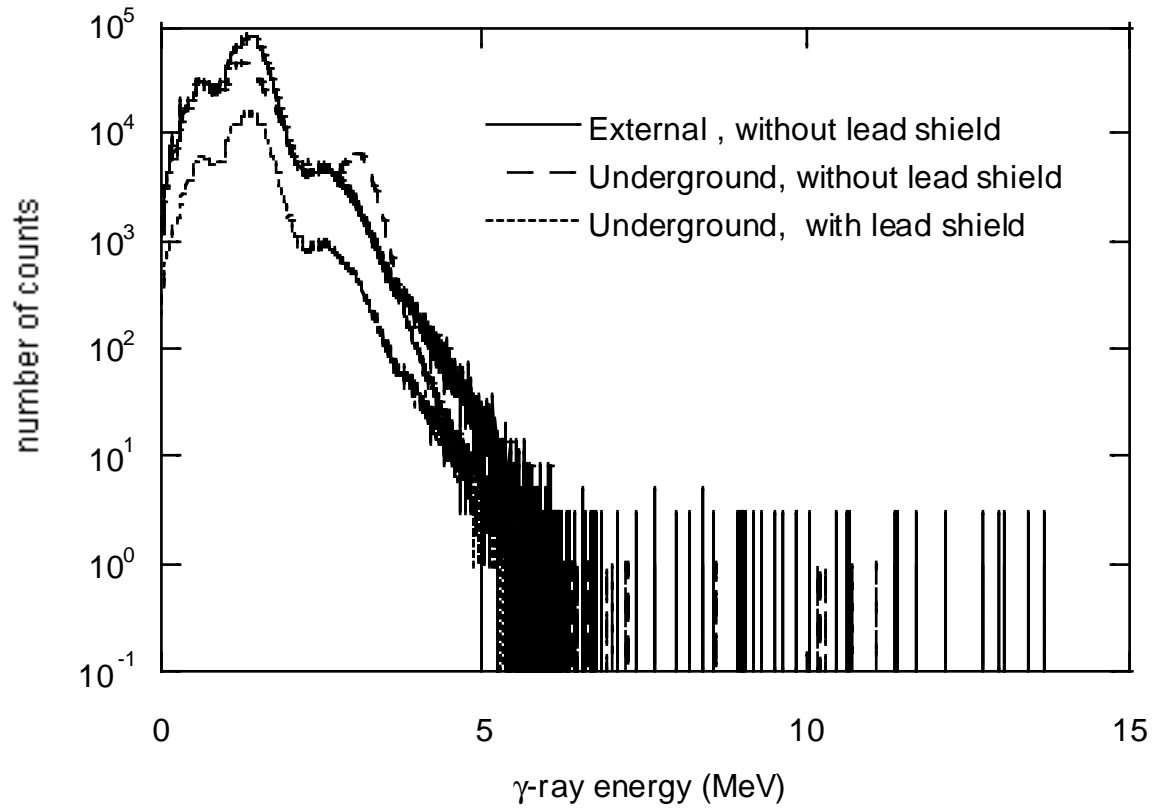
Figure 8

Figure 9

Figure 10